A study of ^{23}Na and ^{12}C
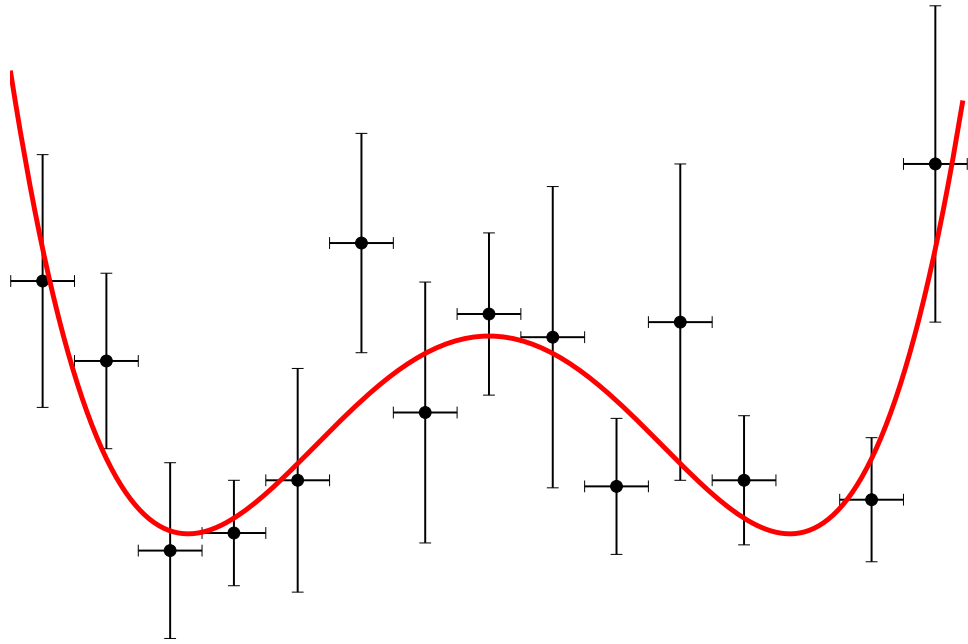
QUALIFICATION EXAM
MICHAEL KULMBACK MUNCH

SUPERVISOR: HANS O. U. FYNBO
CHRISTIAN DIGET

18TH MAY 2016

The front page illustration shows the measured angular correlation between the two photons of the Hoyle state γ cascade. See chapter 5 for details.

Contents

Preface

This progress report details some of the work that I have done during the first half of my Ph.D. studies. I have had the opportunity to participate in multiple experiments at international user facilities as well as performing experiments at the Aarhus University 5 MV Van de Graaff accelerator.

Since nuclear experiments are a complex matter, a significant part of my work has been of a technical nature: developing an analysis and simulation framework and upgrading our data acquisition capabilities. Hence I will present some of the progress I have made in these areas. Fortunately not all the work has been technical, so I will also present the two main physics results.

I would like to extend my gratitude to the Aarhus Subatomic physics group for their support and guidance. Furthermore, I'm thankful for Anne-Sofie Greve who proofread this manuscript.

Experiments:

- IS507, ISOLDE, CERN: *Study of the beta-decay of 20Mg*

- IS575, ISOLDE, CERN: *β-3p spectroscopy and proton-gamma width determination in the decay of 31Ar*

- IS605, ISOLDE, CERN: *Absolute measurement of the beta-alpha decay of 16N*

- PR228, iThemba labs, South Africa: *Measurement of the Hoyle state pair decay and the triple-alpha reaction rate*

- GSFMA332, ANL, USA: *Independent measurement of the radiative branching ratio of the Hoyle state in 12C using Gammasphere*

Publications:

- M. Munch, M. Alcorta, H. O. U. Fynbo *et al. Independent measurement of the Hoyle state β feeding from 12B using Gammasphere.* Physical Review C (in press).
  arXiv: 1601.02853

- A. M. Howard, M. Munch, H. O. U. Fynbo *et al.* ^{23}Na$(\alpha, p)^{26}$Mg *Reaction Rate at Astrophysically Relevant Energies.* Physical Review Letters 115 (2015), 052701.
  DOI: 10.1103/PhysRevLett.115.052701

- J. J. W. H. Sørensen, M. K. Pedersen, M. Munch *et al. Exploring the quantum speed limit with computer games.* Nature, 532 (2016), 210–213.[1]
  DOI: 10.1038/nature17620

- M. Stachura, A. Gottberg, K. Johnston *et al. Versatile Ion-polarized Techniques On-line (VITO) experiment at ISOLDE-CERN.* Nuclear Instruments and Methods in Physics Research Section B: Beam Interactions with Materials and Atoms, 376 (2016), 369–373.[2]
  DOI: 10.1016/j.nimb.2016.02.030

---

[1]Related to my work as a student programmer for `scienceathome.org`
[2]Related to my work as a CERN summer student

1 | Introduction

Take one part nuclear physics experiments and theories, one part astronomical observation and stir them together with stellar and cosmological models at high temperature for $\sim 10^{10}$ years and you will have nuclear astrophysics. Generally speaking, nuclear astrophysics combines the results from these disciplines in order to understand the origin and evolution of the chemical elements and the energy production in stars. My work has been in experimental nuclear physics, which will be the focus of this report.
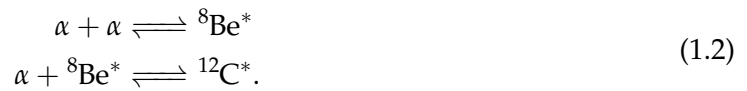
Stellar nucleosynthesis

From astronomical observations one can deduce that the early Universe was primarily seeded with hydrogen and helium in a ratio roughly 3:1 [1]. From these gas clouds the first stars formed by gravitational contraction. This contraction raises the temperature and will continue until fusion reactions in the core become feasible at which point the radiation pressure will stabilize the contraction [2]. The elements in the core are fully ionized and according to classical electro dynamics the Coulomb repulsion would hinder such reactions. It is, however, possible for a particle to tunnel through the Coulomb barrier. The probability for quantum tunneling grows exponentially with energy, while the probability for having a high energy particle drops off rapidly. Combined, these two effects give rise to the Gamow peak, which is a narrow energy window, where fusion can take place.

As the Coulomb barrier for protons is the smallest; hydrogen burning is the first reaction to ignite. At low temperature, this primarily proceeds via the pp reaction network, which effectively fuses four protons into an α particle

$$4p \to {}^4\text{He} + 2e^+ + 2\nu_e. \tag{1.1}$$

At higher temperature hydrogen is burned in the CNO cycle, provided these elements are present in the core.

When a star has exhausted its core of hydrogen, it will contract. If the star is massive enough, i.e. has mass of 0.5-20 solar masses, the contraction raises the temperature enough for helium to be burned in the core. This happens in the two step so-called triple-α reaction

$$\begin{aligned} \alpha + \alpha &\rightleftharpoons {}^8\text{Be}^* \\ \alpha + {}^8\text{Be}^* &\rightleftharpoons {}^{12}\text{C}^*. \end{aligned} \tag{1.2}$$

Since both ${}^8\text{Be}$ and ${}^{12}\text{C}^*$ are unstable, an equilibrium will be established. The leak of this equilibrium happens with the ${}^{12}\text{C}^*$ γ decaying to the stable ground state.

After the helium in the core has been depleted, the star will contract further allowing for carbon, neon and oxygen burning at a later stage. At this point, it might be possible to burn hydrogen and helium in shells.

The Aarhus facility

It would be fantastic to study the triple-α reaction directly in the laboratory, but the densities required make this unfeasible, if not impossible. Instead, one studies the inverse reaction ${}^{12}\text{C}^* \to 3\alpha$, where excited states are populated using various reactions such a ${}^{12}\text{B} \to {}^{12}\text{C}^* + \beta^-$, ${}^3\text{He} + {}^9\text{Be}$ and $p + {}^{11}\text{B}$.

At Aarhus University we have a $5\,\text{MV}$ Van de Graaff accelerator at our disposal. This accelerator can produce beams of either protons, ${}^3\text{He}$ or ${}^4\text{He}$. In this regard, we are very similar

to facilities, which have been operating since the sixties. However, it is the detection system that distinguishes us. Here, we employ multiple large double-sided silicon strip detectors (DSSDs), were each has a solid angle coverage of the order 10%. This allows efficient detection of multi-particle final states such as the three alphas from $^{12}C^*$.

As the name suggests, a DSSD is a solid state detector, where each side consists of multiple strips. Figure 1.1 shows a sketch of our most used detectors: the quadratic W1 and annular S3. With the strips on each side orthogonal to those on the other side, the detector is effectively a pixel detector. However, in order to determine which pixel is hit, it is necessary to determine which strip-pairs match together. This can be done in several ways, but the general procedure is called matching.

We use the Aarhus 5 MV accelerator to populate a state of interest by bombarding a target foil. This will create an excited state, which rapidly decays. The decay products are detected in the DSSDs and from their pixel positions and the deposited energy, one can determine the momentum of the particle, assuming one knows the particle species. From this, one can infer properties of the populated states. Using these properties and time inversion arguments one can determine the stellar reaction rate as a function of temperature.

This report

In this report, I will first summarize the technical work I have performed for the Aarhus 5 MV accelerator; namely upgrading the data acquisition system and writing an analysis framework, AUSAlib, for DSSD detectors. After this I will report on an study of $^{23}Na(\alpha, p)$ performed with the Aarhus 5 MV accelerator in November 2014. Then I will turn to my analysis of an experiment, which was performed with Gammasphere at Argonne National Laboratory, and the preparations for improving the result of this analysis. Lastly, I will briefly summarize the planned work for the next two years.
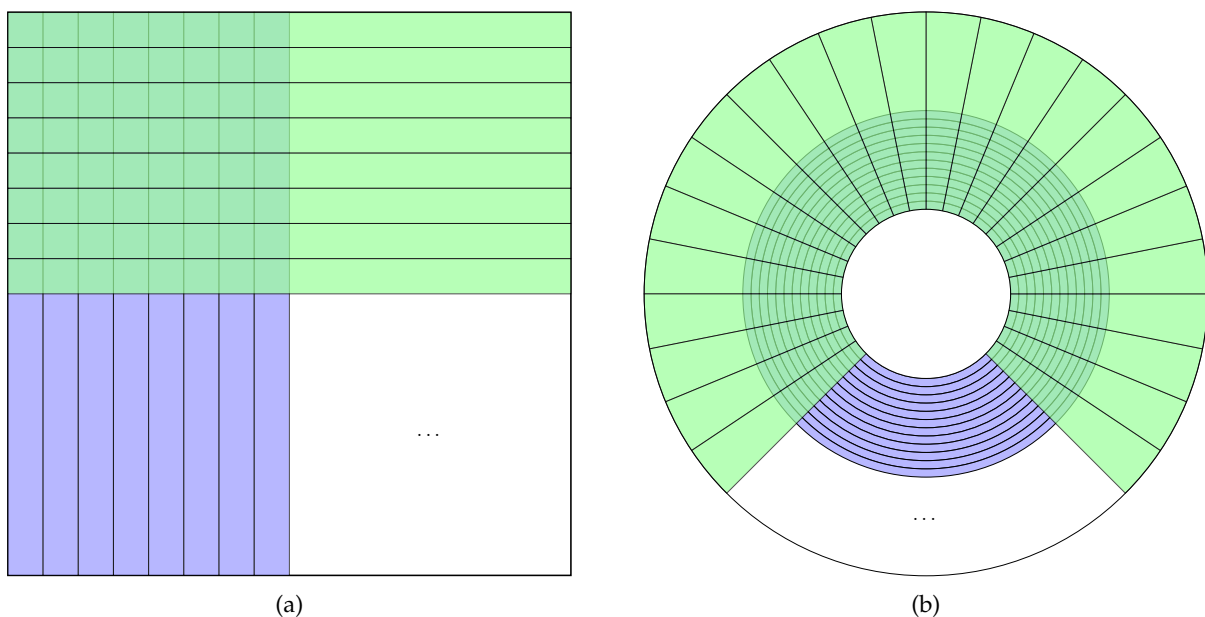

Figure 1.1: Schematic drawing of a W1 (a) and S3 (b) detector. The W1 measures 5 by 5 cm and consists of 16 by 16 strips arranged in a grid. The S3 has an inner diameter of 22 mm, an outer diameter of 70 mm and consists of 24 rings and 32 spokes.

2 | Data acquisition

The data acquisition system (DAQ) is an essential part of any physics experiment. It needs to operate reliably and consistent in order to ensure the quality of the data.

Most DAQ systems can be divided into an analog chain, a digital chain and a read-out system. In this chapter the mode of operation of the analog and digital chain will be described, and afterward I will present requirements for the read-out system. Ultimately the implementation of these requirements will be presented.

2.1 The analog chain

The purpose of the analog chain is to prepare the detector signal for digitization by the digital chain. This process is broken into multiple steps.

2.1.1 Pre amplification

At the Aarhus 5 MV accelerator mainly silicon detectors are employed for charge particle detection. At room temperature a silicon detector will on average create $E/_{3.62\,\mathrm{eV}}$ electron hole pairs due to ionization [3]. For a 3 MeV particle this amounts roughly to 0.1 pC. Such a small signal is *very* prone to noise and should be amplified close to the source.

The amplification is done with a charge amplifier, which integrates the current on a capacitor. This simultaneously acts as a charge-to-voltage converter with an output voltage proportional to the particle energy. However, in order to make the amplifier reusable the capacitor is slowly discharging. This gives pulses with a sharp rise but a long tail of the order 40-60 µs, which can prove a problem with high rates due to multiple pulses summing [3].

The `mesytec MPR 32/64` charge amplifier is used in Aarhus [4].

2.1.2 Amplification

A secondary amplification step that serves several purposes is placed after the pre amplification. It applies an adjustable gain, which is tuned to match the range of the digital chain. Secondarily, the signal is shaped in order to improve the signal to noise ratio. This is essentially a bandwidth narrowing. At the output stage the signal has an extension of 3-4 µs. This sets the hard limit for the maximum rate per input channel.

2.1.3 Discrimination

The discriminators are used for selecting interesting signals. In this context interesting means a signal above a certain height, since low amplitude signals are mainly due to noise. There exists many different techniques for discrimination; two of them are used in Aarhus: Leading edge discriminators perform a comparison with a fixed threshold, while a constant fraction discriminator detects a zero crossing between the input signal and the inverted, scaled and delayed input.

For amplification and discrimination the `mesytec MSCF-16` and `STM16+` modules are used [5, 6]

2.2 The digital chain

The purpose of the digital chain is to digitize the information stored in the analog signal. These data acquisition modules (DAMs) encode different information such as shape, timing, amplitude etc.

Since the digital chain together with the read-out system is normally the bottleneck understanding these modules is key to perform optimizations.

2.2.1 Analog-to-digital converter

While all modules of the digital chain performs analog-to-digital conversion, it is normally the peak sensing analog-to-digital converter (ADC) people refer to as an ADC. It encodes the amplitude of the amplified signal, which is proportional to the deposited energy.

At Aarhus the `CAEN V785` is used to perform the conversion [7]. The main principle of operation is charging of a capacitor with a constant current, while the input potential is larger than the capacitor potential. The potential across the capacitor is subsequently digitized. This requires limit of integration, a `GATE`, in the form of a logic `true` signal, while the integration should be performed. This `GATE` should cover the entire analog signal of the order 3-4 μs.

During the digitization and subsequent capacitor discharging, this module cannot accept new events until after 5.7 μs of the `GATE` - it is `BUSY`. Together with the extension of the `GATE` this sets the hard limit of 100 kHz maximum rate.

2.2.2 Time to Digital converter

One of the main techniques used at the Aarhus facility is studying reactions with multiple reaction products. The interaction time of these products will be almost identical since they originate from the same reaction. On the contrary, background events such as scattered beam particles will arrive at a random time with respect to the reaction products.

A time-to-digital converter (TDC) is used for time stamping the arrival of incoming logic signals. These logic signals are conveniently generated by the discriminators. There exist multiple techniques for performing the time digitization, but it is usually a combination of counting clock cycles and performing interpolation [3].

This is also the case for the `CAEN V1190` which is used at Aarhus [8, 9]. It stores the arrival time of incoming pulses in a cyclic buffer, and when it receives a `TRIGGER` it will look through this buffer and write all timestamps, which have arrived at most some programmable time before the trigger, into an output buffer. This allows an almost `BUSY` free operation. The main concern is overflowing buffers.

2.2.3 Scaler

In order to measure absolute cross sections it is important to know the number of beam particles the target has been subjected to. This is done with a beam digitizer which will output a logic `true` signal per ~ 10 pC.

The number of logic pulses is counted using a scaler module. At Aarhus the `CAEN V830` module is used [10]. It will keep the sum of logic pulses in internal registers and write the current value to an output buffer, when it receives a `TRIGGER`. The write operation takes 1 μs during which the module is `BUSY` and will not accept another `TRIGGER`. However, this will not be the bottleneck, since it happens roughly a factor 10 faster than the ADC conversion.

2.3 The readout system

The readout system serves a dual purpose. First it must select interesting events (triggering), secondarily it transfers the data from the DAMs to persistent storage.
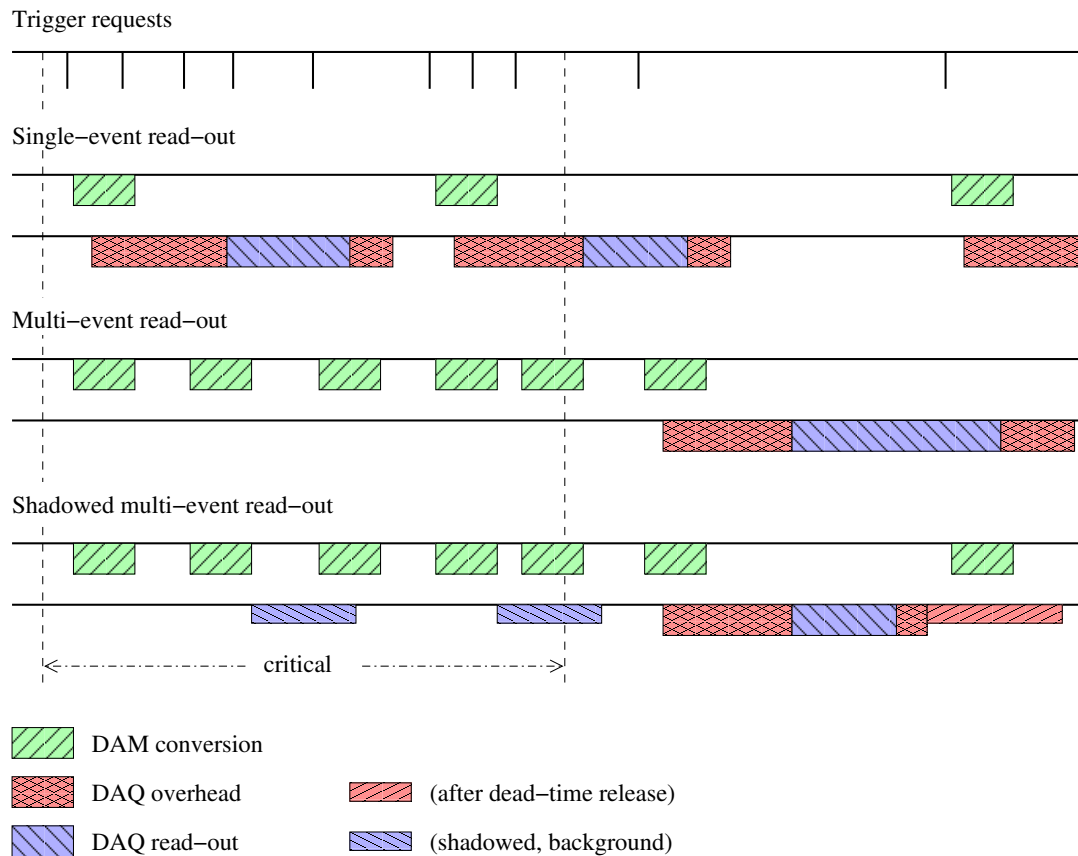
Figure 2.1: Graphical comparison. In single-event mode a readout is performed for each event, while the readout is performed in bunches in multi-event mode. In shadowed read-out mode the readout is performed continuously. The latter two modes are capable of handling spikes in the event rate (marked critical). Figure courtesy of H. T. Johansson [11].

2.3.1   Modes of operation

There are generally three modes of operation for the readout system [11]. A graphical comparison between the multiple modes can be seen on fig. 2.1.

Single-event mode   is the simplest mode to operate. In this mode an event will be read out, once it has been acquired by the DAMs. In the mean time no new events will be accepted. This incurs the overhead of signaling the read-out system for every single event.

Multi-event mode   uses the buffers in the DAMs in order to acquire multiple events before signaling the read-out system. This amortizes the cost of signaling the read-out system. Furthermore, this allows one to use direct memory access, which is more efficient at transferring large data quantities.

Shadowed multi-event read-out mode   performs continuous polling and readout while acquiring data. This avoids the overhead of signaling the read-out system, such that the limiting factor will be the DAM digitization time (marked with green on fig. 2.1).

2.3.2   Existing system

The existing read-out system at the 5 MV accelerator was based on the Daresbury Multi Instance Data Acquisition System (MIDAS). The readout was performed by a `Motorola MVME5500` single

board computer. `TRIGGER` generation was done with NIM logic units, while readout requests and `BUSY` veto was done with the Silena 9418 Acquisition Control module. The main advantage of this system is that no programming is required, since it already supports the CAEN modules. However, multi-event mode is only possible with Silena 9418 modules.

2.3.3 Requirements

As multi-particle final-states is the main objective, it should be possible to acquire data only if the there is a signal in multiple detectors. This can be implemented with an `AND` condition between multiple detectors. However, for crosschecks and normalization one might want to collect single-particle data as well. This can then be done with a downscaled `OR` trigger i.e. accepting every N^{th} single detector trigger. This requires the trigger type to be written into the data stream.

Furthermore, running in multi-event mode requires a component keeping track on the number of accepted triggers since last readout in order to avoid buffer overflow.

2.3.4 Improved DAQ

Most of the requirements can be satisfied by performing the trigger logic and read-out control with a `Vulom4b` module produced by GSI [12]. In terms of hardware, it is a VME board equipped with a Virtex 4 field programmable logic array (FPGA), which features numerous logic in- and outputs on the front panel. The logic, which has previously been implemented using NIM modules, can then be implemented using code, thereby avoiding "cable clutter".

In principle one is free to program the FPGA as one sees fit, however, there already exists tried and tested firmware for the `Vulom`. The TRLO II firmware allows one to define up to 16 different trigger conditions based on 20 inputs [13, 14]. Each of these can be downscaled with a known factor, while the trigger type is recorded and can be accessed via the VME interface. It performs deadtime locking, meaning it will respect the `BUSY` signals from the DAMs and ignore any triggers occurring in the mean time. The number of total and accepted triggers is recorded and made available to the read-out system. Additionally, it has built-in support for running in multi-event mode.

Due to `Vulom` and TRLO II originating from GSI, they are build with the Multi Branch System (MBS) DAQ in mind [15]. MBS is flexible and can scale from single crate experiments to a multi-tier system. MBS handles data packaging, network transport etc., but implementing the readout is left to the user. This is advantageous since it allows for experimentation and fine tuning. On the other hand it is more demanding on the user than MIDAS.

Currently, multiple libraries for performing the actual readout, exist, but `nurdlib` (previously known as `vmelib`) was chosen due to its flexible configuration [16].

At the time of writing, the Aarhus DAQ is running MBS with `nurdlib` in multi-event mode. In the near future the actual VME transfer will most likely be performed using direct memory access, but there is still a few details to work out. The first experiments with performing shadowed read-out mode have been performed, but there is still some work to be done. It is critical to ensure that the detector resolution is not affected by simultaneous VME transfer.

2.4 Summary

In its current shape, the DAQ at the Aarhus 5 MV accelerator is constructed as follows. The detector signal is amplified using pre amplifiers. The signal is further shaped and amplified using the amplifiers, which furthermore performs discrimination. The previous NIM logic has been replaced with a `Vulom` logic board, which performs the trigger logic and acquisition control. The MIDAS read-out system has been replaced with MBS combined with the `nurdlib` readout library.

3 | AUSAlib

Aarhus **Su**batomic **lib**rary

Due to the amount of data collected in a typical experiment, the data must be analyzed using computer programs. Previously the modus operandi of the group was for everyone more or less build their analysis from scratch. While this procedure ensures everyone understands the analysis process, it is also very time consuming and prone to errors.

In the group people are currently working on data from experiments at various international user facilities besides the Aarhus 5 MV accelerator, but while these experiments differ in many aspects, the analysis share some common traits. In order to build a successful library it must suit the needs of all these different experiments.

A big part of the development was agreeing on an analysis process: How to go from raw data to analysis? In the end, we settled on the process outlined in fig. 3.1, where raw data is first unpacked to ROOT files using the `ucesb` tool [17]. Afterwards, it is calibrated and matched before handed to the user for analysis. While the unpacking and sorting can be done experiment independent, the analysis is necessarily very experiment dependent. For this AUSAlib provides the user with additional tools.

I have been in charge of and written most of AUSAlib, and in this chapter I will go into details with some of the design decisions of AUSAlib and what it provides the user.

3.1 Detectors

A key part of any nuclear physics experiment is some sort of detector. One of the common traits in our experiments are the use of double-sided silicon strip detectors (DSSDs), possibly backed by a silicon pad detector. Occasionally, single-sided silicon strip detectors (SSSDs) and germanium detectors have also been employed.

All of these detectors can be neatly classified as either a `DoubleSidedDetector` (DSD) or a `SingleSidedDetector` as shown in fig. 3.2. These two classes then expose a generic interface for working with this class of detector. For instance, it is possible to query a `DSD` for the position of a pixel and an algorithm, which performs dead layer corrections, only needs to know that a specific detector is a `DSD` with a x nm thick dead layer.
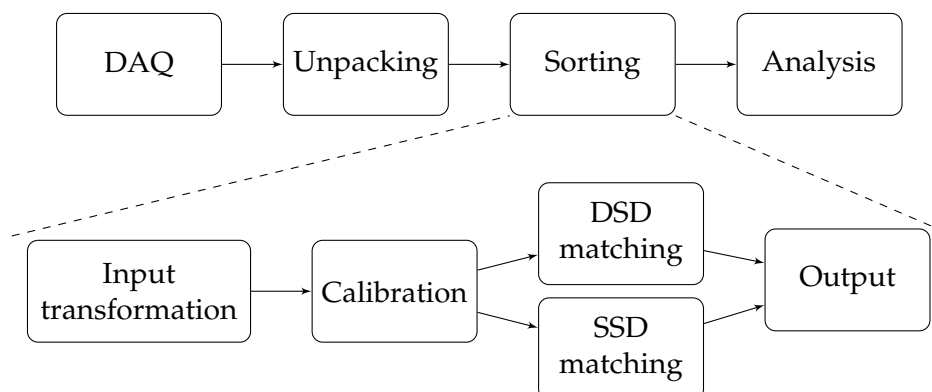

Figure 3.1: Graphical overview of the analysis pipeline. The DAQ will output raw data, which is unpacked and mapped to the detectors using `ucesb`. The unpacked data is then read in, possibly transformed, calibrated from channel numbers to energy. A matching algorithm is then applied to all detectors and afterwards the output is written to file.
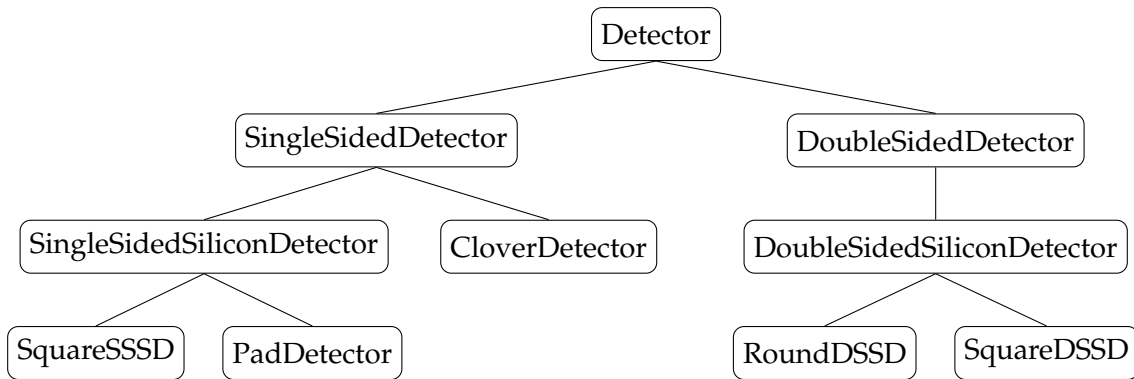
Figure 3.2: Detector inheritance graph

Introducing a new type of detector is then a matter of subclassing an appropriate super class and all algorithms written for these two categories can be applied to the new detector as well. This design is a core part of AUSAlib, which allows users to inject code into standard algorithms. This concept is usually referred to as "change by addition" [18].

3.2 Sorting

With a clearly defined concept of detectors, it is possible to alleviate the user from manually calibrating and matching their data.

Figure 3.3(a) shows the difference in energy between the front and back strips of a W1 detector. This shows a clear Gaussian profile. From this, one can establish a cutoff at which a front/back combination is not considered a pair. For a single hit in the front and back of a detector this matching is easy. Simply compare the difference to the threshold. For multiple hits the combination is done based on minimal difference. It should be noted that this matching works in the majority of cases.

However, there is also the possibility that a particle hits the inter-strip region leading to charge sharing. For a detector of the W1 design, the inter-strip area consists of roughly 1% of the surface area, so this effect is currently neglected. A secondary effect is pileup. This is shown
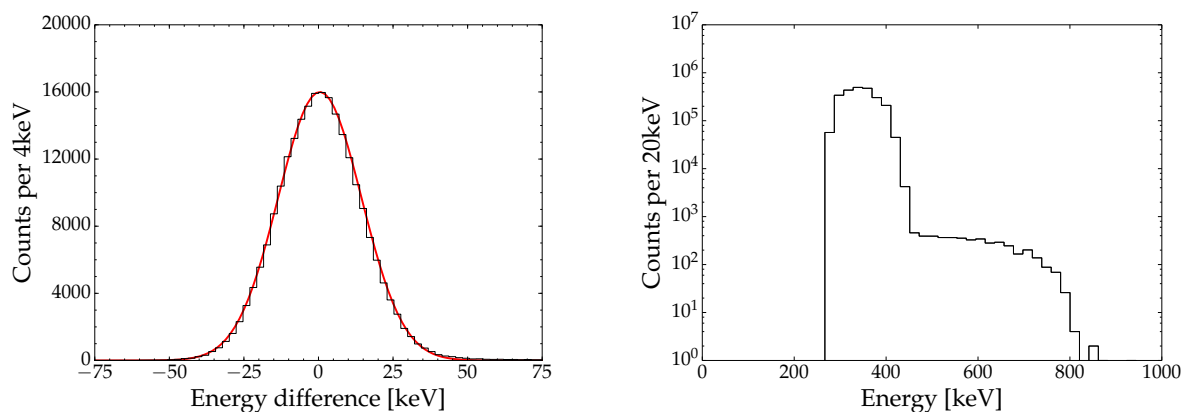
(a) Energy difference between matched front and back strips. The histogram is fitted with a Gaussian distribution, which gives a resolution of 33 keV at FWHM.

(b) Unmatched energy spectrum. The peak is elastically scattered particles while the plateau is due to pileup. Notice the plateau ends at two times the peak energy. In this case 2 ‰ of all events is contained in the plateau.
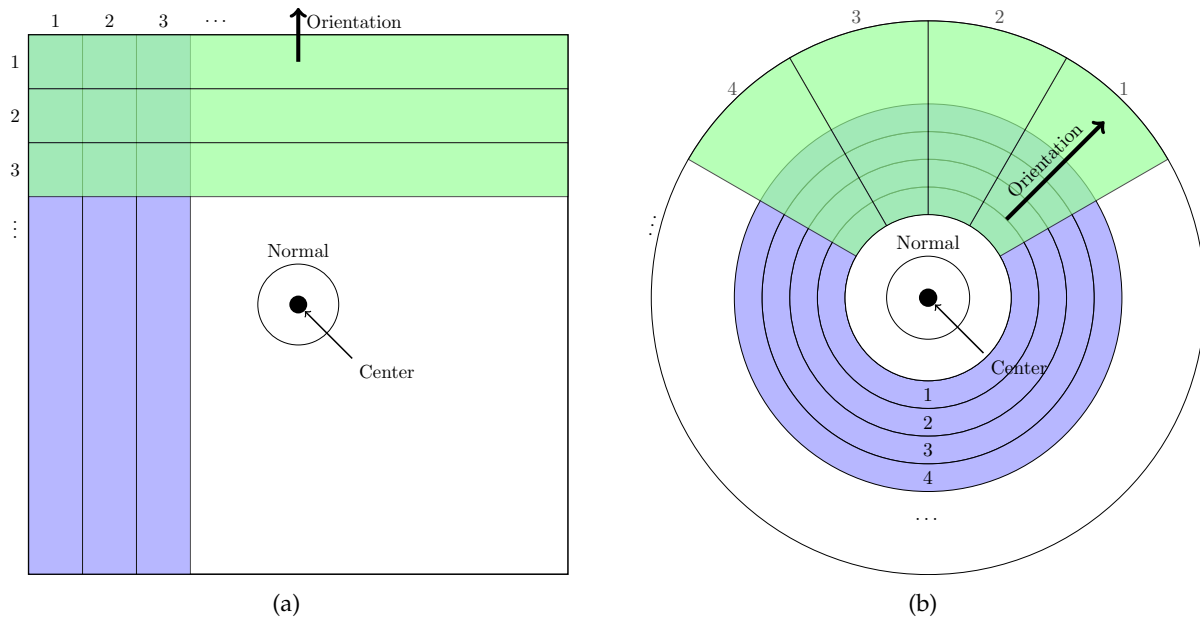
Figure 3.3

Figure 3.4: Schematic drawing of a W1 (a) and S3 (b) detector. For both of them one must supply three vectors, orientation, position and normal, from which the pixel positions are calculated. The normal pertrudes out of the plane. The dots should be taken litterally as AUSAlib does not enforce a specific number of strips.

in fig. 3.3(b) and is caused by two particles hitting the same strip. If they hit two different strips on the backside, then it should be possible to reconstruct the individual energies. However, when reconstructing events one must be careful not to introduce artifacts, so these algorithms are still in development.

Figure 3.1 shows a graphical outline of the sorting step. This is build on the assumption that for each detector side one can construct, via a possible input transformation, a zero suppressed input for each detector side. Each of these inputs contains an array of segment numbers, ADC- and TDC values. A linear calibration is then applied to the ADC values, afterwards the input is matched. The only constraint placed on the matching routine is that the number of entries for the front and back of a DSD should be equal afterwards, and the user is free to replace the default with a specialized algorithm. The default algorithm applies the simple matching described above while also applying thresholds. An extended version is also in development which aligns TDC values. After the matching has been performed, the result is written to a ROOT file and is ready for analysis.

3.3   Setup file

A key feature of any framework is ease of use. To this end, a simple text configuration file was developed. The basic information, which must be provided for a detector, is shown in listing 3.1. The detector geometry is calculated from three vectors: the center, normal and orientation. The interpretation of the orientation vector is detector specific as can be seen in fig. 3.4. For a W1 detector it is defined as the direction of small front strip numbers. For a S3 detector it is defined as the center of strip 1. Additional detector information such as dead layer thickness, number of strips etc. is contained in a stand-alone file, which is kept in a common repository. Combined with a unique ID for each detector this encourages information sharing.

The setup file is one of the core features in AUSAlib as it encapsulates an entire detection system in a single file. It allows the group members to easily participate in analysis of multiple

Listing 3.1: Example from setup file describing a W1 detector located at (33, 0, 0)mm facing in the negative x direction.

```
1  {"name"         : "Det",
2   "file"         : "AUW1_60_00.json",
3   "calibration"  : "Det.cal",
4   "position"     : {"x": "33 mm", "y": "0 mm", "z": "0 mm"},
5   "normal"       : {"x": "−1 mm", "y": "0 mm", "z": "0 mm"},
6   "orientation"  : {"x": " 0 mm", "y": "1 mm", "z": "0 mm"},
7   "frontMapping": {"prefix": "DETF",
8                    "multiplicity": "", "segment": "I",
9                    "tdc": "_T",          "adc": "_E"},
10  "backMapping":  {"prefix": "DETB",
11                   "multiplicity": "", "segment": "I",
12                   "tdc": "_T",          "adc": "_E"},
13 }
```

experiments. Furthermore, several tools have been developed for tasks such calibration, position determination, dead layer calibration etc. Common for all of the tools is the detector geometry must be known. When this is provided in a file, these tools can be easily be shared within the group.

3.4   simX

As analysis programs becomes more complex the potential for error increases. On possible way to deal with this is analysis of simulated datasets. To this end, Oliver Kirsebom and I have build simX, which is a nuclear reaction simulation tool.

Internally a nuclear reaction is described using a tree structure, where each node represents a sub-reaction. With this general structure compound reactions, two-body decay and N-body decays is implemented and can be combined. At each step it is possible to take angular correlations, excitation energies and decay widths into account. simX furthermore simulates the particle detection.

In order to perform a simulation the user must provide a reaction description, beam properties and a AUSAlib setup file and from this simX will produce a file with a structure identical to the unpacked files. Hence the simulated data can be process using the normal analysis pipeline.

Besides analysis cross checks, simX is also used in preparation of an experiment, where it is used to optimize the detector geometry for high efficiency. It is also used during the analysis to determine the detector efficiency.

3.5   Summary

Besides the functionalities listed here AUSAlib provides additional tools for energy calibration, geometry calibration, energy loss etc. and it is used from the very start of the experiment up to and including the physics analysis. An additional project performing on-line analysis have also been build with AUSAlib.

An important design goal is to provide a template algorithm for the user, while allowing the user to important override steps with a custom implementation if needed.

A the time of writing most of the group have adopted AUSAlib as their analysis framework.

4 | ^{23}Na$(\alpha, p)^{26}$Mg

In this chapter I will review an experimental study of the ^{23}Na(α, p) reaction, which we performed in the end of 2014 in order to crosscheck the results published in Ref. [19]. These results were reported in Ref. [20].

4.1 Motivation

The Big Bang hypothesis is, currently, the best model for the evolution of the Universe. It is supported by the observation of the cosmic microwave background, the cosmic expansion and primordial nucleosynthesis. Primordial nucleosynthesis is the fusion of protons and neutrons into heavier elements in a timescale shorter than the half-life of the neutron. This seeded the Universe predominantly with H and He in a 3:1 ratio [1].

From this seed the first generation of stars was formed. In their interior, hydrogen or helium were slowly fused into even heavier elements. Through various mechanisms these elements were then reintroduced back into the inter-stellar medium from which new generations of stars were formed. Hence, younger stars are "polluted" with metals, which can be observed in their photosphere.

While intriguing, this is essentially an indirect measurement of ongoing nucleosynthesis. The first direct evidence was provided by the HEAO-3 satellite in 1984, which observed the 1809 keV gamma line from the galactic center [21]. This gamma line is emitted by the first excited state ^{26}Mg, which is populated by the β decay of the ^{26}Al ground state with a half-life of 1.04×10^6 yr. As this is much shorter than the age of the Universe ($\sim 10^{10}$ yr) it serves as direct proof of ongoing nucleosynthesis [22].

While later observations have linked ^{26}Al to massive stars, the main source has not yet been identified [22]. There are currently several candidates, but the models all depend on nuclear reaction rates. In a paper from 2011 Illiadis *et al.* investigated the ^{26}Al production sensitivity to various reaction rates and found that a factor of 10 increase in the reaction rate of ^{23}Na(α, p) would increase production by a factor of 3 [23].

This was explored in an inverse-kinematics experiment by Almaraz-Calderon *et al.* [19], which claimed a factor of 40 increase compared to previous experiments [24, 25] and statistical model calculations [26]. Almaraz-Calderon *et al.* claimed that the discrepancy was due to target degradation in earlier experiments, which employed an intense α beam.

4.2 Experiment

The reaction mechanism used in this experiment is shown in fig. 4.1(a). Using a beam of α particles excited states in ^{27}Al are populated. These can subsequently decay to ^{26}Mg via proton emission with a Q-value of 1.821 MeV. With the available beam energies the accessible states in ^{26}Mg are the ground state and the first excited state at 1.809 MeV. There also exists a state at 2.938 MeV, but the protons from this reaction were very low energetic and could not be detected.

For this experiment two DSSDs were mounted in the scattering chamber as seen in fig. 4.1(b). An annular 322 μm DSSD covered laboratory angles from 140° to 163°, while a quadratic 40 μm DSSD, with a 1500 μm silicon pad detector behind, covered angles between 60° and 120°.
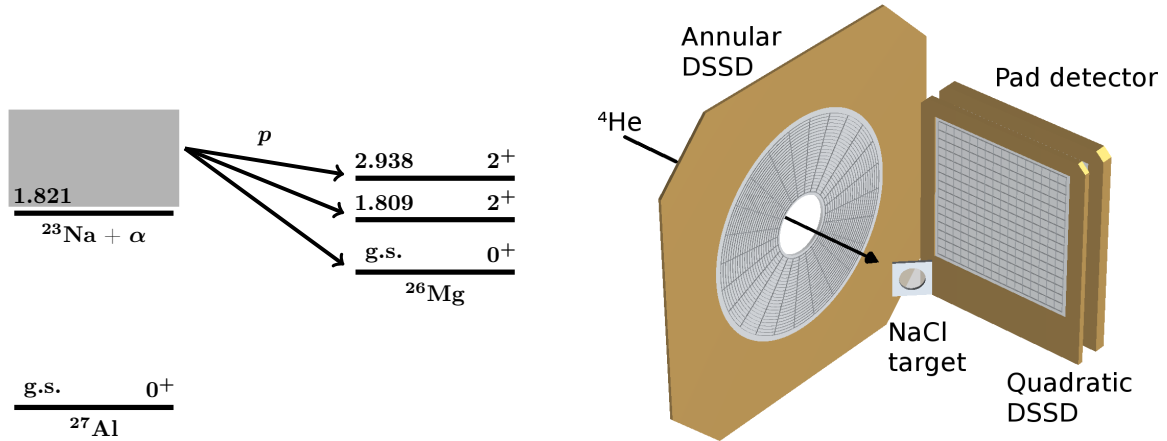
(a) Sketch of the reaction mechanism. Excited states in ^{27}Al are populated and subsequently proton decay to ^{26}Mg. All energies are in MeV relative to the ^{26}Mg ground state.

(b) Schematic drawing of the experimental setup with a quadratic and annular DSSD. The α-particle beam, as indicated by an arrow, impinged on a NaCl target rotated $45°$. Figure courtesy of A. M. Howard [20].

Figure 4.1

The α-particle beam was produced by the 5 MV Van de Graff accelerator, which is capable of producing up to 5 MV beams with a precision of ± 1 keV. The beam current is measured 70 cm downstream in an electrically suppressed Faraday cup connected to a beam digitizer.

The target was prepared at Aarhus University by evaporating natural NaCl onto a $10\,\mu g/cm^2$ carbon foil. In order to determine the thickness accurately it was bombarded with a 3 MeV α-particle beam with the carbon backing facing towards and away from the beam respectively. From the shift in energies a target thickness of $76(7)\,\mu g/cm^2$ was inferred.

For the experiment the target was bombarded with a 200-500 ppA beam of α particles with an energy between 2 and 3 MeV. In order to distinguish the protons from beam particles, the annular detector was rotated $180°$, so a 4 μm dead layer was facing the target. This dead layer acted as a degrader foil, which due to difference in energy loss, increases the energy separation between α particles and protons, as can be seen in the top panel of fig. 4.2. Similar identification was achieved in the quadratic detector, where only protons could punch through and deposit energy in the back detector.
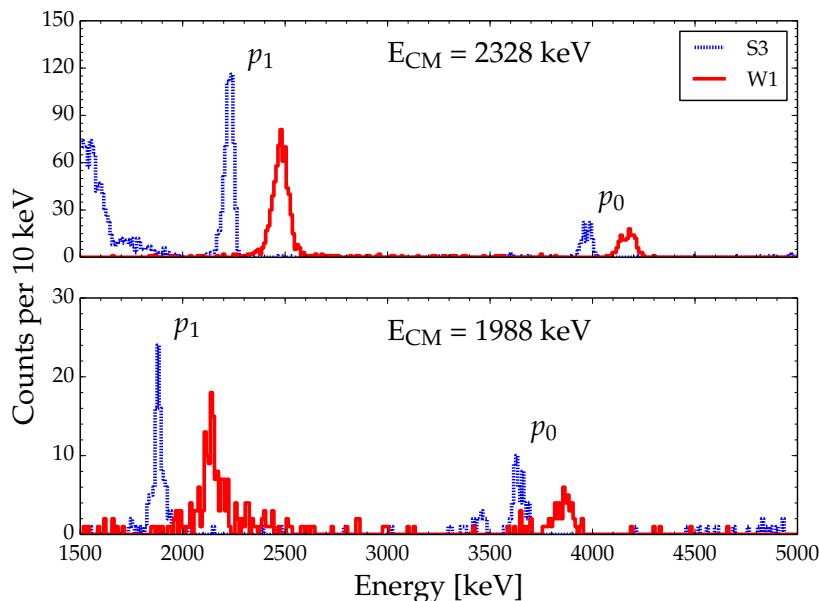

Figure 4.2: Examples of measured energy spectra in the annular (dashed blue) and quadratic (solid red) detector taken at center of mass energies 2328 keV and 1988 keV. In both cases there are two clear peaks in each spetra.
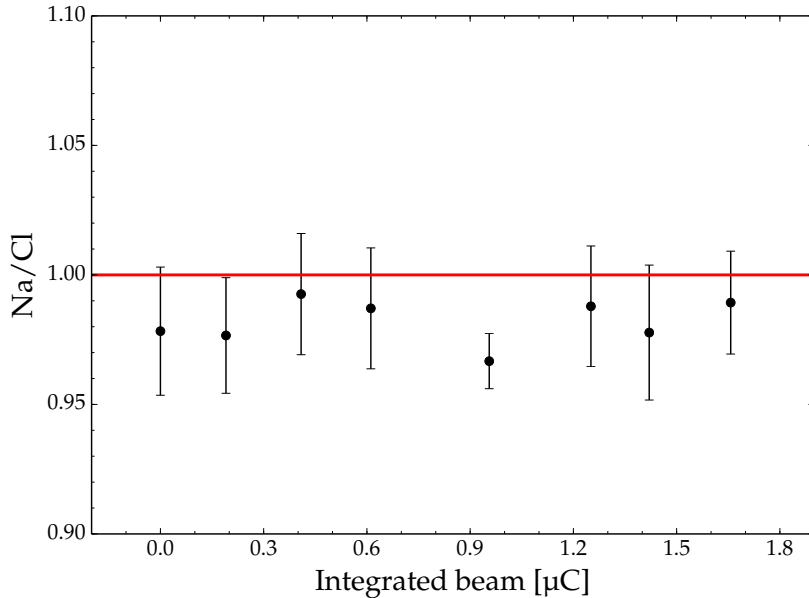
Figure 4.3: Stochiometric ratio of Na and Cl, determined from Rutherford scattering, as a function of integrated beam current.

4.3 Analysis

Almaraz-Calderon *et al.* suggested target degradation as the source of discrepancy with earlier results, so in order to eliminate this potential source of error, the target state was continuously monitored. It has been shown by Cheng *et al.* that ^{23}Na(α, α') is Rutherford distributed up to 3 MeV [27]. Hence, the elastic yield for ^{23}Na and $^{35/37}$Cl was extracted from a single strip of the quadratic detector. The inferred stoichiometric ratio is shown in fig. 4.3. It is clear that our target suffered no degradation.

For the quadratic DSSD the protons can be identified by requiring a signal in the back detector, as only protons are energetic enough to punch through the thin front detector. However, for the outer ring of pixels it was observed that the proton could miss the back detector, hence, these pixels were excluded. This yields the solid red spectra in fig. 4.2.

As noted, the annular detector was mounted such that the dead layer acted as a degrader foil. Without further processing the dashed blue spectra in fig. 4.2 were achieved.

From this appropriate energy cuts could be determined. By applying these and correcting for solid angle the differential angular yield could be determined. This was normalized to the elastic α yield. For pure Rutherford scattering this yield is proportional to the target thickness and stoichiometry. Hence, this removes any uncertainties associated with these being non-constant, in addition to effects related to beam integration.

Examples of the resulting angular distributions for both p_0 and p_1 can be seen in fig. 4.4, where they have been fitted with the three lowest order Legendre polynomials. This assumes symmetry around $90°$, which seems justified from the results reported by Ref. [24], who only found a single resonance to be forward peaked. Nonetheless, a conservative 20% error has been assumed due to this.

However, the measurements at the two lowest energies require special attention. Here the energies of some of the p_1 protons are not high enough to punch through the quadratic detector and are thus excluded from the fit of the angular distribution. Performing the same exclusion at higher energies result in an increase in the cross section between 10% and 30%, hence a 30% uncertainty has been assumed for these two data points.
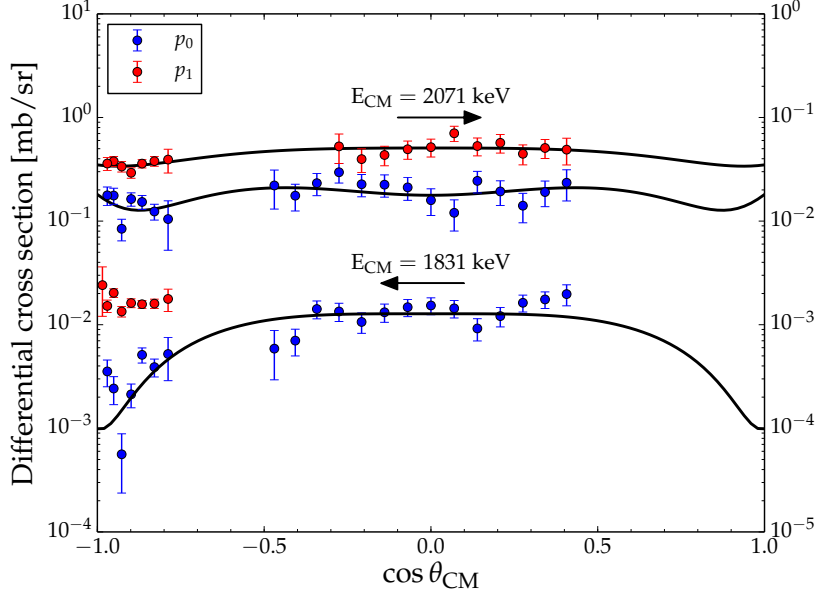
Figure 4.4: Example of measured differential cross sections for p_0 and p_1. For the low energy measurement p_1 could not be detected in the quadratic DSSD. The fitted distribution generally peaks around 90°. The arrows indicates the y-axis for the datasets.
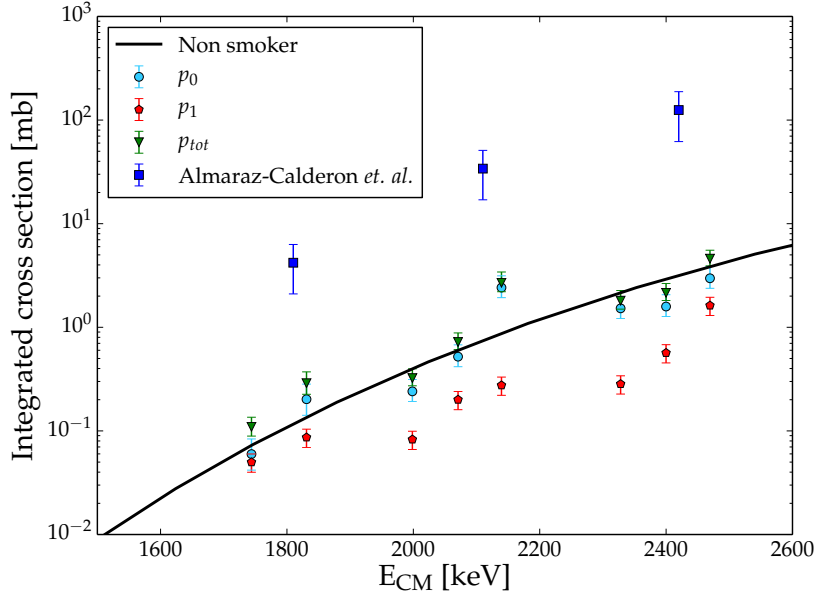

Figure 4.5: Integrated cross sections for the p_0, p_1 and their sum. The results of Almaraz-Calderon et al. is plotted for comparison [19]. The results are clearly inconsistent.

4.4 Discussion

The extracted cross sections for p_0, p_1 and their sum can be seen in fig. 4.5 together with the results from Ref. [19]. The solid line is a calculation based on the statistical model Non-Smoker [26]. As the target is 50-100 keV thick, our data points are associated with effective energies i.e. a weighted average of the energy has been calculated using the Non-Smoker cross section as weight.

From this, it is clear that the results differ from the results of Ref. [19] by more than an order of magnitude. On the other hand, our data agrees with Non-Smoker on both magnitude and trend, with the only exception at $E_{CM} = 2.16$ MeV. However, this coincides with a strong resonance reported by [25]. Keeping the energy dependence of Non-Smoker, an optimum scaling factor between Non-Smoker and our data is found to be 0.96 ± 0.06.

At the time these results were published [20], we could not explain the discrepancy with Ref. [19], however, it could not be explained by their choice of angular distribution as it peaked at

large angles (where they measured), while our measured angular distributions peaked at 90°.

Our results were, however, published simultaneously with a complimentary inverse-kinematics experiment by Tomlinson *et al.* [28], which corroborated our findings. Subsequently, Almaraz-Calderon *et al.* published an erratum; stating that they erroneously did not correct for the beam current detector being downscaled with a factor 100 [29].

Based on this information an updated version of fig. 4.5 can be seen on fig. 4.6. The data from Ref. [19] have been corrected with a factor 100. Furthermore, instead of using their assumed angular distribution, our measured angular distributions have been used. Tomlinson *et al.* assumed an isotropic angular distribution in the analysis of their data, so their data points have been recomputed using our measured distribution. For the data points, at an energy higher than what we measured, the angular distribution associated with the highest energy have been used. As is clearly seen in fig. 4.6 the three datasets are now in agreement and the general trend and magnitude is reproduced by Non-Smoker

4.5   Conclusion

The ^{23}Na(α, p) reaction has been investigated and angular distributions and total cross sections have been extracted. The results are incompatible with the results of Ref. [19], but compatible with their updated results when corrected for the angular distribution [29]. The statistical model Non-Smoker reproduces the trend and magnitude of all three datasets [19, 20, 28, 29] within 30%, except at the strong resonance at $E_{CM} = 2.16\,\mathrm{MeV}$, where the error is roughly 50%. Hence, I recommend the continued usage of this in astrophysical simulations.
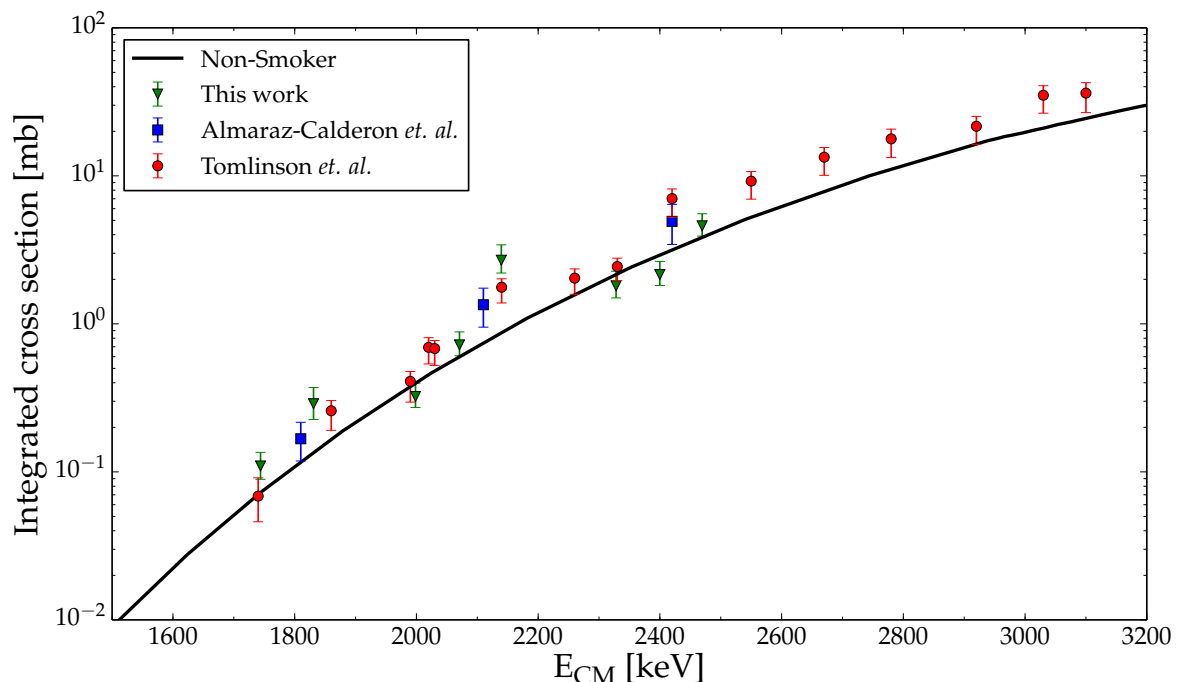

Figure 4.6: Total cross section for ^{23}Na(α, p). The data sets of from Almaraz-Calderon *et al.* [19] and Tomlinson *et al.* [28] have been adjusted. See text for details.

5 | ^{12}B β-branching ratio to the Hoyle state

In this chapter I will review my analysis of an experiment performed at Argonne National Laboratory in 2012 and the planned improvements. The results of this analysis have just been accepted for publication in Physical Review C, so only a preprint is available [30]. M. Alcorta *et al.* have reported on a preliminary analysis of this experiment [31].

5.1 Motivation

The importance of ^{12}C in stellar nucleosynthesis was first realized by Fred Hoyle in a ground breaking paper in 1953 [32]. He conjectured an excited state just above the triple-α threshold, which greatly enhances the helium burning rate in stars with a temperature of 10^8-10^9 K.

The state, which is known as the Hoyle state, is used as a benchmark for nuclear structure theories as it has some quite peculiar characteristics. The results from several state-of-the-art theories have been reviewed by Freer and Fynbo, who found that most of them predicts a collective 2^+ excitation of the Hoyle state to exist in the region of 0.8-2.3 MeV above it [33]. This excitation is interesting for core-collapse supernovae, as it would increase the triple-α reaction rate at $T > 10^9$ K by a factor 5-10 compared to the result of Caughlan *et al.* [34–38].

There have been several experimental studies of the collective excitation since it was first conjectured by Morinaga in 1956 [39]. The region is however dominated by several broad states. The first widely accepted evidence was provided by Freer *et al.*, who used inelastic proton scattering on ^{12}C [38]. Using R-matrix analysis they deducted a 2^+ contribution at 9.6(1) MeV with a width of 600(100) keV. These results were corroborated by Itoh *et al.* using inelastic α scattering [40] and a simultaneous analysis was published subsequently [41]. Results using the alternative population mechanism ^{12}C$(\gamma,\alpha)^8$Be also observed a 2^+, but at $10.13^{+0.06}_{-0.05}$ MeV and with a much larger width of 2080^{+330}_{-260} keV [42, 43]. One could speculate that this might be due to the existence of several 2^+ states in the region, which are being populated with different strength, in the various experiments.

^{12}C has also been studied extensively using the β decay of ^{12}B and ^{12}N [44–49]. Due to the selection rules the 1^+ ground states will predominantly populate even-parity states with spin 0, 1 or 2, and not the strong 3^- state at 9.64 MeV state, which was the main background in the inelastic scattering experiments. However, no β-decay experiment has identified a 2^+ state at 10 MeV. The β-decay spectrum was analyzed using the R-matrix formalism in Ref. [49]. In this analysis both 0^+ and 2^+ strength was observed in the 10.5 MeV to 12 MeV region with recommended resonance energies at 11 MeV. Due to its closeness to the triple-α threshold, the Hoyle state has a large tail extending to high energies. This is known as the "ghost anomaly" [50, 51] and its contribution in the R-matrix analysis depends strongly on the branching ratio by which the Hoyle state is populated in the β decay.

This branching ratio was determined for ^{12}B in the most recent experimental study [48]. Here the beam was implanted in a silicon detector, providing accurate normalization. The result of the analysis was a branching ratio of 0.58(2) %, which is inconsistent with the previously established value of 1.2(3) % (1.5(3) % is listed in Ref. [52], but this should be revised [53]). This reduced branching ratio was used in the subsequent R-matrix analysis [49]. Furthermore, as it is forbidden, by the Pauli principle, to β decay to a pure triple-α cluster state, then a precise
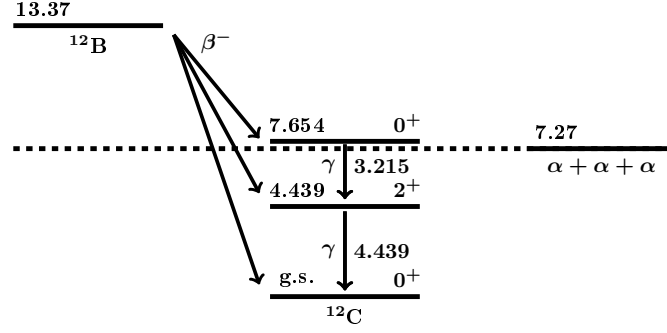
Figure 5.1: Level scheme of ^{12}C with the relevant states. The ^{12}B ground state and triple-α threshold is also shown. Energies are in MeV.

measurement of the branching ratio will provide insight into the cluster breaking component of the wave function. This will be discussed further in section 5.4.

In order to provide experimental confirmation of the result reported in Ref. [48] our experiment provides an independent measurement of the branching ratio using an array of high-purity germanium detectors.

5.2 Experiment

Figure 5.1 shows the decay scheme for the ground state of ^{12}B to the relevant states in ^{12}C. The first excited state is below the threshold for α emission and hence can only γ decay. The Hoyle state cannot γ decay directly to the ground state, but a cascade decay via the first excited state is allowed. Hence, it is possible to detect the Hoyle state γ decay by simultaneously detecting a 3215 keV and 4439 keV photon. From this, the branching ratio to the Hoyle state and its relative γ width can be determined by normalizing to the decay of the first excited state

$$\text{BR}(7.65)\frac{\Gamma_\gamma}{\Gamma} = \text{BR}(4.44)\frac{N_{\gamma\gamma}}{N_{4.44}\epsilon_{3.21}C_\theta}, \tag{5.1}$$

where $N_{\gamma\gamma}$ is the number of coincidence events, $\epsilon_{3.21}$ the efficiency for detecting a 3215 keV photon and C_θ corrects for the angular correlation between the two photons.

The weighted average for the relative radiative width has been computed using the values compiled by Obst *et al.* [54], but excluding the data point from Seeger *et al.* as it is a clear outlier [55]. From this, the relative pair width from Ref. [33] has been subtracted; yielding a relative γ width $\frac{\Gamma_\gamma}{\Gamma} = 4.07(11) \times 10^{-4}$.

The experiment was performed at the Argonne Tandem-Linac Accelerator System (ATLAS) located at Argonne National Laboratory, which provided a pulsed (40 ms on, 40 ms off) 40 MeV ^{11}B beam that impinged on a deuterated titanium foil (TiD$_2$), sufficiently thick to stop the beam. ^{12}B was hence produced in inverse kinematics by ^{11}B$(d,p)^{12}$B. The target was manufactured according to the method discussed in Ref. [56] and it contained approximately 1.5 mg/cm^2 deuterium (estimated by weight).

The Gammasphere array of 110 high-purity Compton-suppressed germanium detectors, of which 98 where operational, was used to detect photons; yielding almost 4π coverage. The trigger for the DAQ was operated in singles mode, meaning a hit in any detector could trigger the acquisition. Data was only collected during beam off.

5.3 Analysis

Figure 5.2 shows the entire γ spectrum, which was collected over 67 hours. A clear peak at $4439.5 \pm 0.7(\text{sys})$ keV (A) corresponding to the decay of the first excited state in ^{12}C is easily
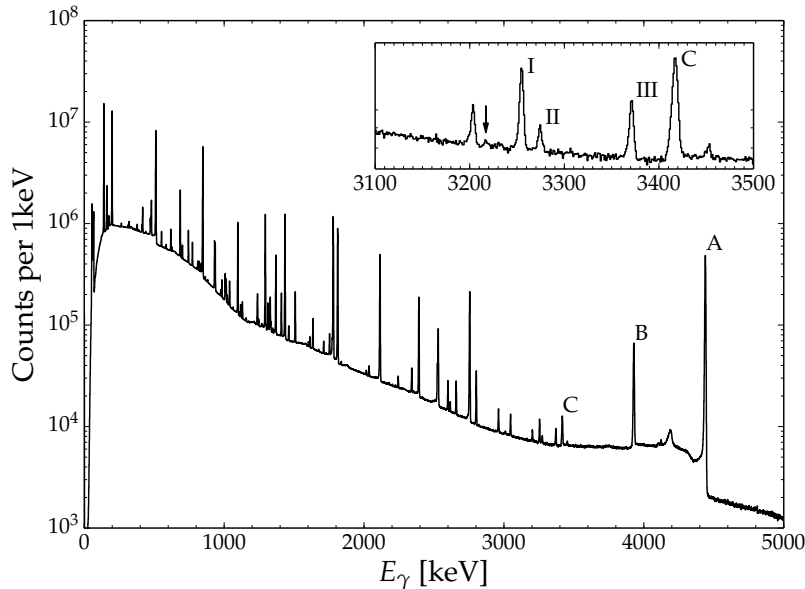
Figure 5.2: Entire singles spectrum. The transition from the first excited state (A) and its escape peaks (B,C) are clearly visible. A small structure around 3215 keV is indicated by an arrow in the insert.
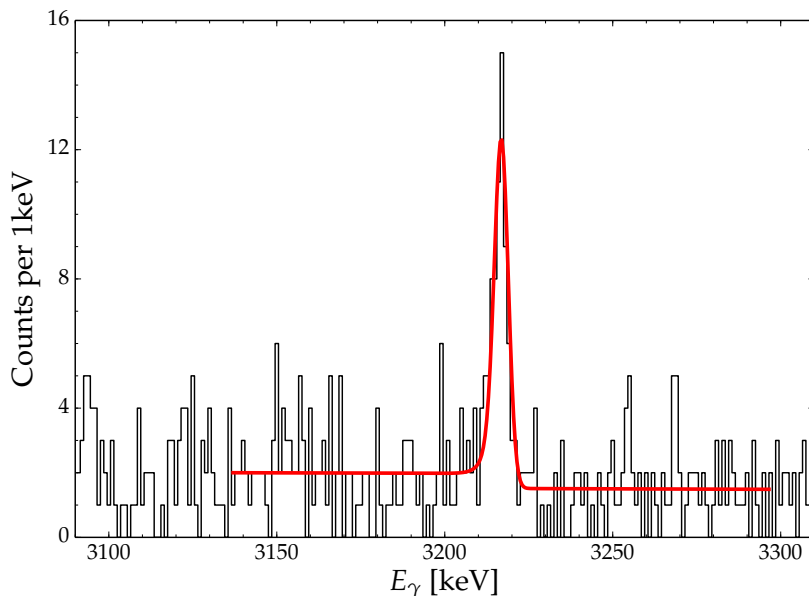

Figure 5.3: Coincidence spectrum produced by gating on the 4439 keV peak and detection time difference. A peak at 3217 keV is clearly visible. See the text for details of the fit.

identified together with its first (B) and second escape peak (C). The insert shows the 3.1 to 3.5 MeV region, where a small structure, marked by an arrow, is visible around 3215 keV. Furthermore, the three peaks marked I-III has been identified as coming from ^{56}Mn and ^{56}Co produced by in-beam reactions with Ti.

In order to determine the number of decays from the first excited state the peak at 4439 keV was fitted with a sum of a Gaussian distribution, a skewed Gaussian distribution, a linear background and a smoothed step function [57]. The fit was performed with MINUIT minimizer using the Poisson log likelihood ratio in order to reduce systematic effects [58, 59]. From this procedure, the area of the peak was determined to be $N_{4.44} = 9.20(2) \times 10^6$, where the error was dominated by uncertainties in the functional form of the peak.

The lifetime of the first excited level is ~ 70 ps, so for a true event the two photon must be detected simultaneously. This requirement was assured by placing a gate on the relative time between the detection of the two photons and requiring that the energy of one should coincide with the energy of the 4439 keV transition. The resulting coincidence spectrum can
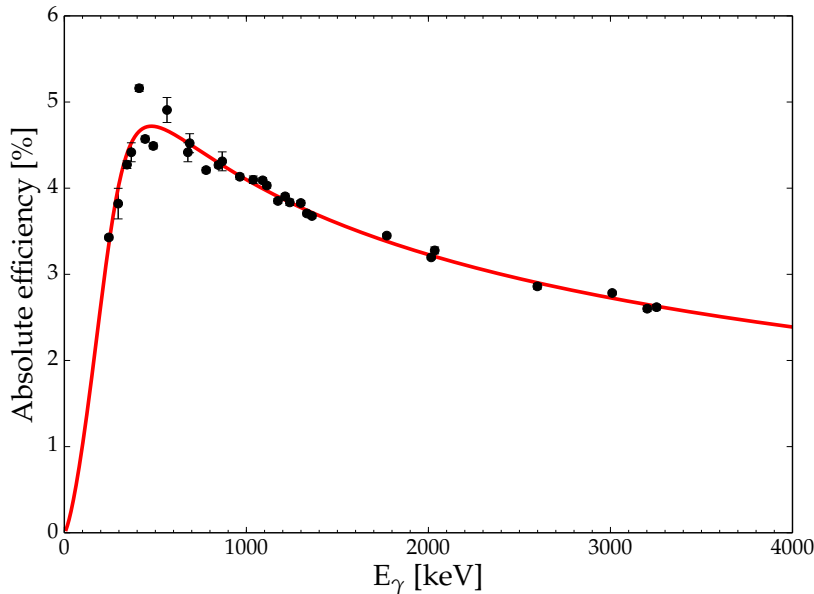
Figure 5.4: Absolute efficiency for all 98 Gammasphere detectors. The relative effieciency is determined from ^{152}Eu and ^{56}Co. The absolute normalization is determined from the cascade decay of ^{60}Co and ^{24}Mg. The error on the fit is smaller than the linewidth.
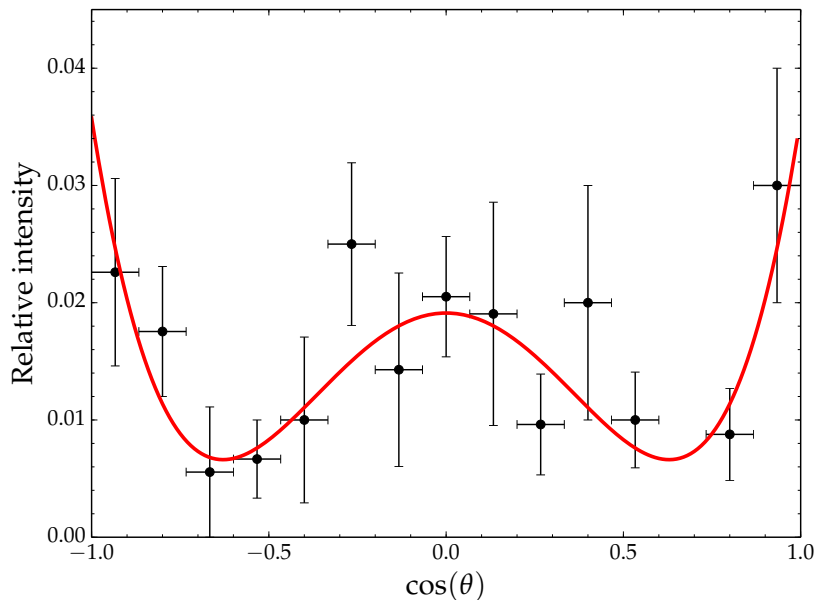

Figure 5.5: Angular correlation between the two photons of the Hoyle state cascade decay. The number of counts have been corrected for the number of detector pairs with a specific angle between them. The solid line is the best fit to eq. (5.2).

be seen in fig. 5.3, which shows a clear peak at $3216.9^{\pm 0.7 (\text{sys})}_{\pm 0.4 (\text{stat})}$ keV. The peak was fitted using the same procedure as before, but the parameters for the skewed Gaussian distribution have been determined from peak I-III in fig. 5.2. The area of the peak, determined from the fit, is $N_{\gamma\gamma} = 58(9)$.

The relative efficiency was determined using the standard calibration sources ^{152}Eu and ^{56}Co mounted at the target position. This provides calibration points, both at low energy and in the important 3 MeV region. In order to provide absolute normalization, the coincidence method described in Ref. [57] was used for the cascade decay of a ^{60}Co source, and for ^{24}Mg. The latter was produced by in-beam reactions; most likely ^{11}B with oxygen. As the ^{60}Co source was quite strong, it was necessary to correct for random coincidences, the number of which was determined by selecting the events fulfilling the energy requirement, but not the time requirement. After correcting for this, the absolute efficiency at 3217 keV was determined to be $\epsilon_{3.21} = 2.94(2)\%$.

The angular correlation between the two photons in the cascade decay has not previously

been measured. However, with the excellent angular coverage of Gammasphere this was possible. The events were selected using the gates described previously and additionally requiring the energy of the second γ ray to be within $10\,\text{keV}$ of $3217\,\text{keV}$. The background was estimated by gating outside of the peak and the shape of it was found to be flat. The angular correlation, corrected for the geometric efficiency (number of detector pairs with a specific angle between them) can be seen in fig. 5.5 together with the best fit to

$$W(\theta) = k\left[1 + a_2\cos^2\theta + a_4\cos^4\theta\right], \tag{5.2}$$

where θ is the angle between the two γ rays. The best fit is achieved with $a_2 = -3.3(7)$ and $a_4 = 4.2(9)$, which is consistent with the theoretical expectation $a_2 = -3$ and $a_4 = 4$ for a $0 \rightarrow 2 \rightarrow 0$ cascade [60].

With the theoretical angular correlation confirmed, it can be used to compute C_θ in eq. (5.1). This is done with a simple Monte Carlo simulation of the detector setup.

5.4   Discussion

The Hoyle state is highly clustered, however, a β decay to a pure α-cluster state from either ^{12}B or ^{12}N is forbidden due to the Pauli principle [61]. Hence, the branching ratio yields a sensitive probe of the α-cluster-breaking component of the Hoyle state wave function. In current state-of-the-art nuclear structure theories, such as Fermionic Molecular Dynamics (FMD) [62, 63] and Antisymmetrized Molecular Dynamics (AMD) [61], this is modeled by mixing shell-model-like (i.e. single particle) wave functions with α-cluster states. The effect of the α-cluster breaking in ^{12}C was investigated recently using such a hybrid shell/cluster model [64], which found the spin-orbit force to strongly effect excited 0^+ states.

In order to compare our results with these models the $\log ft$ value is computed. The phase-space factor (f factor) is calculated using the parametrization given in Ref. [65]. The current established half-life of $20.20(20)$ ms is used [52]. From this we arrive at the result

$$\log ft = 4.50(7), \tag{5.3}$$

which is incompatible with the result of AMD calculations $\log ft = 4.3$.

Hence, the branching ratio measured by us and Hyldegaard *et al.* [48] indicates that the α clustering of the Hoyle state is more pronounced than previously believed. One could therefore speculate that this could reduce the chance of observing the collective excitations of the Hoyle state in β-decay studies. The results of updated AMD/FMD calculations, which reproduced the revised branching ratio to the Hoyle state, would be quite interesting.

5.5   Conclusion and outlook

The β-decay branching ratio from ^{12}B to the Hoyle state has been measured using an array of high-purity germanium detectors, providing an independent measurement with different systematic uncertainties than the most recent experimental study [48]. The result is consistent with the results of Ref. [48], but a factor ~ 2 smaller than the previously-established literature value. This updated branching ratio was used to calculate $\log ft = 4.50(7)$, which is inconsistent with the result of AMD calculations. Our branching ratio indicates that the α clustering of the Hoyle state is more pronounced than previously believed.

The angular correlation of the photons, in the Hoyle state cascade decay, has also been measured. The result is consistent with theoretical expectations [60].

The errors of this measurement are dominated by the counting statistics on the number of coincidences; contributing 91% of the total error. In comparison, the uncertainty on the β-decay-branching ratio to the first excited state contributes 6% and the relative γ width 2%.

By increasing statistics one could perform a $\sim 6\%$ measurement of either the γ width or the β-decay-branching ratio.

The limiting factor in this experiment, in terms of beam current, was neutron damage to Gammasphere. These neutrons were mainly produced in reactions with titanium, as the beam energy was above the Coulomb barrier. Exchanging titanium for hafnium would allow running higher beam currents with substantially less background. We have entered into a collaboration with Jacques Chevallier and the Center for Materials Crystallography at Department of Chemistry in order to produce deuterated hafnium targets. Furthermore, as a recent development it should be possible to only acquire data during beam off with the improved Gammasphere DAQ [66].

Combined, these improvements mean one could run a more intense beam with a lower background rate and less DAQ dead time.

6 | Outlook

If we start at ANL and Gammasphere; the experiment and analysis is done. However, we have entered into a collaboration in order to produce deuterated hafnium targets. The first targets have yet to be produced, but we plan to measure the deuterium depth profile using the procedure outlined in Ref. [67] first at the Aarhus 5 MV accelerator and then possibly at CMAM near Madrid. If this proves promising, we will apply for beam time at ANL.

The data acquisition system have been upgraded, while the Aarhus 5 MV accelerator have been down for maintenance since July 2015. As the current system fulfills most of our requirements, and the accelerator is more or less up and running, my attention will turn towards physics.

At the time of writing we will most likely start with $^7\text{Li}(p, \gamma)$, where we would like to study the γ decay of the 17.6 MeV state in ^8Be. This γ decay will be studied indirectly, by detecting all charged particles. Since a specific resonance is populated one can infer a γ decay from the energy missing from the charged particles. The main background is ^7Li breakup into ^3He and ^4He and elastically scattered beam particles, however with a fairly large γ-branching ratio $\sim 10^{-3}$ the γ decay should be quite easy to identify.

The γ decay of 17.6 MeV state is of interest in the context of $^9\text{Be}(^3\text{He}, \alpha)^8\text{Be}$, where we want to study the γ decay of the doublet at ~ 16.8 MeV, which is related to the ^8B neutrino spectrum via the Conserved Vector Current hypothesis [68, 69]. The branching ratio for the γ decay of this doublet is of the order 10^{-5}, so here the 17.6 MeV state will serve as a guide line, especially since ^3He induces significantly more background reactions.

Furthermore, we also want to study the decay of broad states in ^{12}C. These will be populated using the well-known $^{11}\text{B} + p \rightarrow {}^{12}\text{C}$ reaction. By populating well-known high lying resonances and using the γ decay to selectively probe states with a certain spin and parity [70], the hope is that this will provide some additional information on the newly observed 2^+ state at ~ 10 MeV, which was also the motivation for chapter 5.

This fall I will be traveling to York University, where I will be staying for a semester. Among other things the plan is to study the $^7\text{Li}(\gamma, t)\alpha$ reaction, for which inconsistencies were identified in a recent theoretical study [71].
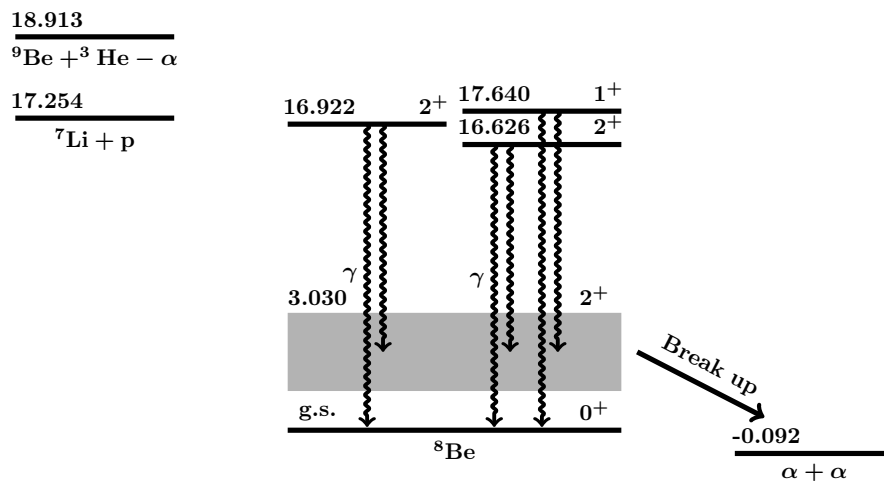
Figure 6.1: Excited states of ^8Be are populated using either $^9\text{Be}(^3\text{He}, \alpha)^8\text{Be}$ or $^7\text{Li} + p$. In both cases γ rays are detected indirectly from missing energy of the charged particle.

Bibliography

[1] A. Coc, J.-P. Uzan, and E. Vangioni. *J. Cosmol. Astropart. Phys.* 2014 (2014), p. 50. DOI: 10.1088/1475-7516/2014/10/050. arXiv: 1403.6694.

[2] C. A. Bertulani and T. Kajino (2016), p. 88. arXiv: 1604.03197.

[3] W. R. Leo. *Techniques for Nuclear and Particle Physics Experiments: A How-to Approach.* Springer, 1994. ISBN: 3540572805.

[4] *MPR-16/L data sheet.* v. 7.0_01. mesytec. URL: http://www.mesytec.com/products/datasheets/MPR-16.pdf.

[5] *MSCF-16 data sheet.* v. 51_01. mesytec. URL: http://mesytec.com/products/datasheets/MSCF16-F-V.pdf.

[6] *STM16+ data sheet.* v. 2.4_01. mesytec. URL: http://www.mesytec.com/products/datasheets/STM-16+.pdf.

[7] *V785 data sheet.* Rev. 13. CAEN S.p.A. Dec. 2012. URL: http://www.caen.it/servlet/checkCaenManualFile?Id=8888.

[8] *V1190 data sheet.* Rev. 13. CAEN S.p.A. July 2012. URL: http://www.caen.it/servlet/checkCaenManualFile?Id=8657.

[9] *HPTDC - High Performance Time to Digital Converter.* Version 2.2. CERN. Mar. 2004. URL: https://cds.cern.ch/record/1067476.

[10] *V830 data sheet.* Rev. 4. CAEN S.p.A. Jan. 2007. URL: http://www.caen.it/servlet/checkCaenManualFile?Id=5281.

[11] H. T. Johansson. "The DAQ always runs". Lic. Thesis. Chalmers University of Technology, 2006. ISBN: 978-91-7385-360-6.

[12] J. Hoffman. *Vulom4B data sheet.* Accessed: 2016-04-08. Feb. 2013. URL: https://www.gsi.de/fileadmin/EE/Module/VULOM/vulom4B_3.pdf.

[13] H. T. Johansson et al. *GSI Sci. Rep.* 2010, p. 231.

[14] H. T. Johansson et al. *GSI Sci. Rep.* 2013, p. 354. DOI: 10.15120/GR-2014-1-FG-S-FRS-15.

[15] H. G. Essel and N. Kurz. *Nuclear Science, IEEE Transactions on* 47 (2000), pp. 337–339. DOI: 10.1109/23.846176.

[16] B. Löher et al. *GSI Sci. Rep.* 8. 2014, p. 192. DOI: 10.15120/GR-2015-1-MU-NUSTAR-NR-08.

[17] H. T. Johansson. *The ucesb unpacker generator.* Accessed: 2016-05-11. 2010. URL: http://fy.chalmers.se/~f96hajo/ucesb/ucesb_doc.pdf.

[18] H. B. Christensen. *Flexible, Reliable Software: Using Patterns and Agile Development.* 1st. Chapman & Hall/CRC, 2010. ISBN: 978-14-2009-362-9.

[19] S. Almaraz-Calderon et al. *Phys. Rev. Lett.* 112 (2014), p. 152701. DOI: 10.1103/PhysRevLett.112.152701.

[20] A. M. Howard et al. *Phys. Rev. Lett.* 115 (2015), p. 052701. DOI: 10.1103/PhysRevLett.115.052701. arXiv: 1506.05983.

[21] W. A. Mahoney et al. *Astrophys. J.* 262 (1982), p. 742. DOI: 10.1086/160469.

[22] R. Diehl. *Rep. Prog. Phys.* 76 (2013), p. 026301.
DOI: 10.1088/0034-4885/76/2/026301.

[23] C. Iliadis et al. *Astrophys. J. Suppl. Ser.* 193 (2011), p. 16.
DOI: 10.1088/0067-0049/193/1/16.

[24] J. Kuperus, P. Glaudemans, and P. Endt. *Physica* 29 (1963), pp. 1281–1295.
DOI: 10.1016/S0031-8914(63)80237-2.

[25] D. P. Whitmire and C. N. Davids. *Phys. Rev. C* 9 (1974), pp. 996–1001.
DOI: 10.1103/PhysRevC.9.996.

[26] T. Rauscher and F.-K. Thielemann. *At. Data Nucl. Data Tables* 79 (2001), pp. 47–64.
DOI: 10.1006/adnd.2001.0863.

[27] H.-s. Cheng, X.-y. Lee, and F. Yang. *Nucl. Instrum. Methods Phys. Res. Section B* 56-57 (1991), pp. 749–752.
DOI: 10.1016/0168-583X(91)95018-9.

[28] J. R. Tomlinson et al. *Phys. Rev. Lett.* 115 (2015), p. 052702.
DOI: 10.1103/PhysRevLett.115.052702.

[29] S. Almaraz-Calderon et al. *Phys. Rev. Lett.* 115 (2015), p. 179901.
DOI: 10.1103/PhysRevLett.115.179901.

[30] M. Munch et al. *Phys. Rev. C (in press)* (2016). arXiv: 1601.02853.

[31] M. Alcorta et al. *EPJ Web of Conferences*. Vol. 66. EDP Sciences, 2014, p. 07001.
DOI: 10.1051/epjconf/20146607001.

[32] F. Hoyle. *Astrophys. J. Suppl. Ser.* 1 (1954), p. 121.
DOI: 10.1086/190005.

[33] M. Freer and H. Fynbo. *Prog. Part. Nucl. Phys.* 78 (2014), pp. 1–23.
DOI: 10.1016/j.ppnp.2014.06.001.

[34] G. R. Caughlan and W. A. Fowler. *At. Data Nucl. Data Tables* 40 (1988), pp. 283–334.
DOI: 10.1016/0092-640X(88)90009-5.

[35] C. Tur, A. Heger, and S. M. Austin. *Astrophys. J.* 671 (2007), pp. 821–827.
DOI: 10.1086/523095.

[36] C. Tur, A. Heger, and S. M. Austin. *Astrophys. J.* 718 (2010), pp. 357–367.
DOI: 10.1088/0004-637X/718/1/357.

[37] L. The et al. *Astrophys. J.* 504 (1998), pp. 500–515.
DOI: 10.1086/306057.

[38] M. Freer et al. *Phys. Rev. C* 80 (2009), p. 041303.
DOI: 10.1103/PhysRevC.80.041303.

[39] H. Morinaga. *Phys. Rev.* 101 (1956), pp. 254–258.
DOI: 10.1103/PhysRev.101.254.

[40] M. Itoh et al. *Phys. Rev. C* 84 (2011), p. 054308.
DOI: 10.1103/PhysRevC.84.054308.

[41] M. Freer et al. *Phys. Rev. C* 86 (2012), p. 034320.
DOI: 10.1103/PhysRevC.86.034320.

[42] W. R. Zimmerman et al. *Phys. Rev. Lett.* 110 (2013), p. 152502.
DOI: 10.1103/PhysRevLett.110.152502.

[43] W. R. Zimmerman. "Direct observation of the second 2+ state in 12C". PhD thesis. University of Connecticut, 2013.

[44] C. W. Cook et al. *Phys. Rev.* 107 (1957), pp. 508–515.
DOI: 10.1103/PhysRev.107.508.

[45] D. E. Alburger. *Phys. Rev. C* 16 (1977), pp. 2394–2400.
DOI: 10.1103/PhysRevC.16.2394.

[46] H. O. U. Fynbo et al. *Nature* 433 (2005), pp. 136–9.
DOI: 10.1038/nature03219.

[47] C. Diget et al. *Nucl. Phys. A* 760 (2005), pp. 3–18.
DOI: 10.1016/j.nuclphysa.2005.05.159.

[48] S. Hyldegaard et al. *Phys. Lett. B* 678 (2009), pp. 459–464.
DOI: 10.1016/j.physletb.2009.06.064.

[49] S. Hyldegaard et al. *Phys. Rev. C* 81 (2010), p. 024303.
DOI: 10.1103/PhysRevC.81.024303.

[50] F. C. Barker and P. B. Treacy. *Nuclear Physics* 38 (1962), pp. 33–49.
DOI: 10.1016/0029-5582(62)91014-3.

[51] D. H. Wilkinson et al. *Phys. Rev.* 130 (5 1963), pp. 1953–1960.
DOI: 10.1103/PhysRev.130.1953.

[52] F. Ajzenberg-Selove. *Nucl. Phys. A* 506 (1990), pp. 1–158.
DOI: 10.1016/0375-9474(90)90271-M.

[53] S. Hyldegaard et al. *Phys. Rev. C* 80 (2009), p. 044304.
DOI: 10.1103/PhysRevC.80.044304.

[54] A. W. Obst and W. J. Braithwaite. *Phys. Rev. C* 13 (1976), pp. 2033–2043.
DOI: 10.1103/PhysRevC.13.2033.

[55] P. Seeger and R. Kavanagh. *Nuclear Physics* 46 (1963), pp. 577–597.
DOI: 10.1016/0029-5582(63)90630-8.

[56] J. P. Greene, H. Young Lee, and H.-W. Becker. *Nucl. Instrum. Methods Phys. Res., Sect. A* 613 (2010), pp. 462–464.
DOI: 10.1016/j.nima.2009.10.004.

[57] K. Siegbahn. *Alpha, Beta and Gamma Ray Spectroscopy.* Elsevier Science Ltd, 1965. ISBN: 072040083X.

[58] U. Bergmann and K. Riisager. *Nucl. Instrum. Methods Phys. Res., Sect. A* 489 (2002), pp. 444–447.
DOI: 10.1016/S0168-9002(02)00864-1.

[59] F. James and M. Roos. *Comput. Phys. Commun.* 10 (1975), pp. 343–367.
DOI: 10.1016/0010-4655(75)90039-9.

[60] E. L. Brady and M. Deutsch. *Phys. Rev.* 72 (1947), pp. 870–871.
DOI: 10.1103/PhysRev.72.870.

[61] Y. Kanada-En'yo. *Progress of Theoretical Physics* 117 (2007), pp. 655–680.
DOI: 10.1143/PTP.117.655.

[62] R. Roth et al. *Nucl. Phys. A* 745 (2004), pp. 3–33.
DOI: 10.1016/j.nuclphysa.2004.08.024. arXiv: nucl-th/0406021.

[63] M. Chernykh et al. *Phys. Rev. Lett.* 98 (2007), p. 032501.
DOI: 10.1103/PhysRevLett.98.032501.

[64] T. Suhara and Y. Kanada-En'yo. *Phys. Rev. C* 91 (2015), p. 024315.
DOI: 10.1103/PhysRevC.91.024315.

[65] D. Wilkinson and B. Macefield. *Nucl. Phys. A* 232 (1974), pp. 58–92.
      DOI: 10.1016/0375-9474(74)90645-9.

[66] J. T. Anderson et al. *2012 IEEE Nucl. Sci. Symp. Med. Imaging Conf. Rec.* IEEE, 2012, pp. 1536–1540. ISBN: 978-1-4673-2030-6.
      DOI: 10.1109/NSSMIC.2012.6551368.

[67] M. Mayer et al. *Nucl. Instrum. Methods Phys. Res., Sect. B* 267 (2009), pp. 506–512.
      DOI: 10.1016/j.nimb.2008.11.033.

[68] L. De Braeckeleer et al. *Phys. Rev. C* 51 (1995), pp. 2778–2788.
      DOI: 10.1103/PhysRevC.51.2778.

[69] A. J. Sørensen. "The Neutrino Spectrum from Boron-8". Cand. Thesis. 2011.

[70] O. S. Kirsebom et al. *J. Phys. Conf. Ser.* 569 (2014), p. 012013.
      DOI: 10.1088/1742-6596/569/1/012013.

[71] T. Neff. *Phys. Rev. Lett.* 106 (2011), p. 042502.
      DOI: 10.1103/PhysRevLett.106.042502.